We are IntechOpen, the world's leading publisher of Open Access books Built by scientists, for scientists

5,000
Open access books available

125,000
International authors and editors

140M
Downloads

Our authors are among the

154
Countries delivered to

TOP 1%
most cited scientists

12.2%
Contributors from top 500 universities

CLARIVATE ANALYTICS
BOOK CITATION INDEX
INDEXED

WEB OF SCIENCE™

Selection of our books indexed in the Book Citation Index
in Web of Science™ Core Collection (BKCI)

Interested in publishing with us?
Contact book.department@intechopen.com

Numbers displayed above are based on latest data collected.
For more information visit www.intechopen.com

A Review of Classic Torque Control Techniques for Switched Reluctance Motors

Marcelo Vinícius de Paula, Tárcio André dos Santos Barros and Pedro José Dos Santos Neto

Abstract

In this chapter, the most relevant electronic torque control methods established in the current literature are addressed. The electronic torque control methods are divided into two technical topologies. The first one aims to control the average torque produced by the switched reluctance machine and is ideal for applications that require wide speed range of operation. The second topology enrolls the instantaneous torque production and is required in low torque ripple applications. Different torque control methods are addressed, for instance, direct average torque control, current profiling through torque sharing functions, direct torque control, and direct instantaneous torque control. Detailed information regarding the working principle and implementation of the methods is presented. Mathematical simulations are conducted in Matlab/Simulink® environment to elucidate the methods. Finally, a comparison of all addressed methods regarding the torque ripple minimization capabilities is presented.

Keywords: instantaneous torque control, average torque control, torque ripple minimization, direct average torque control, current profiling, torque sharing function, direct torque control, direct instantaneous torque control

1. Introduction

Switched reluctance machines (SRMs) main advantages are their simple structure, without coils, and rare materials in the rotor, low cost, ruggedness, brushless operation, operation in high temperature environments, high reliability, fault tolerance, wide speed range of operation, high efficiency and high torque, and power density. These advantages enable SRMs as competitive to more traditional electric machines, such as induction motors, permanent magnet synchronous machines (PMSM), and DC machines in many applications [1, 2].

Besides the advantages, SRMs are strongly dependent in electronic converters for its drive. Also, automatic control of these machines is complex due to nonlinear characteristics. Furthermore, the efficiency and power factor of SRM are generally lower than those of PMSM as a result of higher losses in SRM. The switched reluctance machines have doubly salient structure and nonlinear characteristics, thus, these machines present elevated torque ripple and acoustic noise. These are the predominant disadvantages encountered in SRMs [3, 4].

The scientific community focuses on mitigating these disadvantages through electronic control or through structural changes in the machine. For instance, in [5], the authors analyze the effect of different frames and ribs structure topologies over the acoustic noise production. The methods that target the structural changes consist in manipulating the magnetic flux linkage in such way that the reluctance variation between cycles is smaller, thus resulting in shallower torque ripple. On the other hand, the speed range of operation is diminished because the torque per ampere ratio is also diminished.

In contrast, the electronic control methods aim to minimize the torque ripple by manipulating a set of control parameters, such as electric phase current, turn on angle, turn off angle, and excitation voltage, which regulate the machine operation. These parameters may be controlled directly or indirectly. The electronic control methods will be focused in this chapter.

In order to understand the working principle of the control methods, some other concepts must be addressed initially. In SRMs, the phase inductance (L) varies according to the rotor position (θ) because of the reluctance variation caused mostly by the air-gap changes as the rotor revolves. The inductance profile for a generic four-phase ideal SRM phase is highlighted in **Figure 1(a)**. The pointed angles in the abscissa axle refer to the relative position between a point in the rotor and a point in the stator, where θ_{as} is the start of alignment position, θ_a is the aligned position, θ_{ms} is the start of misalignment position, and θ_m is the misaligned position. These positions and their respective inductance are also pointed in the SRM physical structure in **Figure 1(b)**. The aligned position occurs when the entirety of the rotor pole is bounded by the stator pole, and in this position, the inductance is at its maximum and the reluctance at its minimum. The misaligned position occurs when the entirety of the rotor pole is off the stator pole bounds [6].

Because of its working principle, SRMs require an electronic converter as a driver. The classic and most used topology is the asymmetric half bridge (AHB) [6, 7], which demand two power switches and two power diodes for its construction. There are several other proposed topologies in the literature for specific applications. In [8], the SRM phases are used as components of a charging station. In [9], the authors embed the SRM and AHB components as part of a converter with voltage boosting and power factor correction capabilities. The research presented in [10, 11] apply the SRM windings and AHB components for flexible energy conversion and multi-operation mode of the SRM. The authors in [12] propose an integrated SRM and drive system designed for hybrid energy storage systems composed of batteries and supercapacitors.

The schematic circuit for a three phase AHB is presented in **Figure 2**. This topology may be applied for any number of phases and enables operation in all four
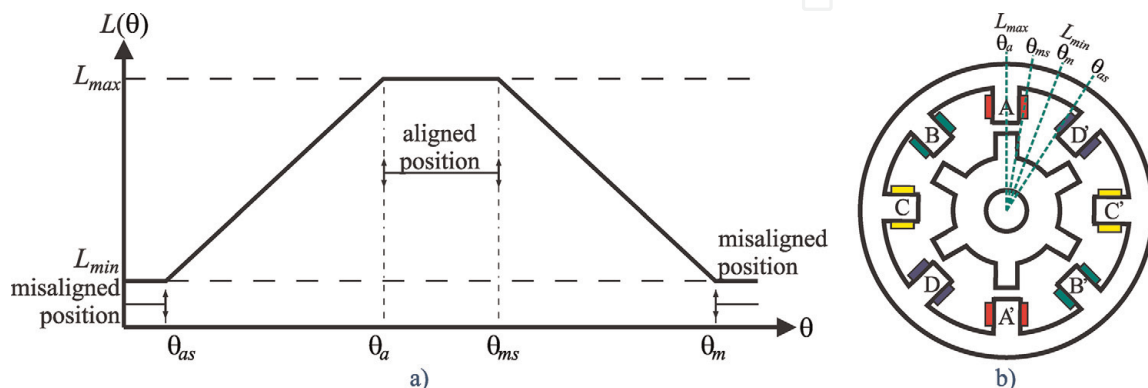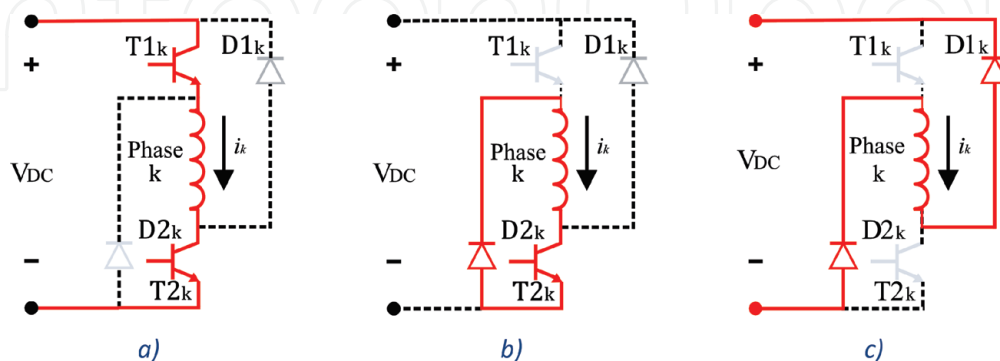

Figure 1.
Inductance variance according to rotor position: (a) inductance profile for one electric cycle of one SRM phase; (b) physical structure of a 8/6 SRM with main rotor position highlighted.
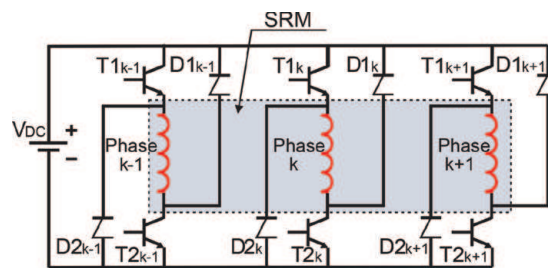
Figure 2.
Schematic circuit of the asymmetric half bridge converter for SRM drive.

Figure 3.
Voltage states for the AHB converter: (a) magnetization or positive state (1), (b) free-wheeling or null state (0), and (c) demagnetization or negative state (−1).

quadrant of the torque-speed plane. The AHB support independent voltage control for all the SRM phases. Three voltage levels are possible according to the power switches states.

Figure 3 shows all three possible voltage states that may be applied to the SRM phases using an AHB converter. In case both switches are conducting, positive voltage is applied to the phase terminals, and this state is known as positive state or magnetization (1) as depicted in **Figure 3(a)**. If only one switch is conducting, null voltage will be applied to phase terminals and the electric current will flow through the circuit formed by the conducting switch, power diode, and SRM phase winding. This state is named free-wheel or null state (0) (**Figure 3(b)**). In case both switches are not conducting, negative voltage is applied to the SRM phase, characterizing the demagnetization or negative state (−1) as depicted in **Figure 3(c)**.

The choice of the driving angles (θ_{on} and θ_{off}) has great influence over the electronic control method applied. Some researches focus on the influence of these angles. The research presented in [13, 14] is focused on optimal angles for applications in current hysteresis control, while in [15], the authors focus the analysis on the voltage single pulse operation. The angle selection may have different objectives, for example, maximizing the efficiency, minimizing torque ripple or minimizing acoustic noise. The majority of the studies present optimizations aiming to minimize torque ripple [16, 17] and/or minimize the losses [18]. For this chapter, the focus will be on minimizing the torque ripple.

When the SRM is working at low speeds and current hysteresis control may be applied, at the beginning of the conduction period, the inductance value is almost constant, and consequently, a small amount of torque is produced. When the stator and rotor poles start to overlap, the torque production rises, thus when the rotor position overcomes the turn-off angle, a negative voltage must be applied to the phase terminals to guarantee that the electric current flowing through the phase reaches zero before the inductance starts to decrease. The magnetic flux linkage rise is constant because of the quazi-linear inductance variation. At the end of the

commutation, the magnetic flux returns to zero because of the negative voltage applied. After that, zero voltage is applied to the phase.

On the other hand, when the SRM is working at high speeds, the back electromotive force (back EMF) is elevated, and the excitation voltage is not enough to guarantee appropriate hysteresis current control. Thus, voltage single pulse control is applied. At the beginning of the conduction interval, the electric current rises because there is voltage being applied to the phase terminals after the rotor position overcome the turn on angle (θ_{on}). At certain point, the back EMF rises and the electric current can no longer increase, thus current hysteresis is inapplicable. The back EMF is directly proportional to the electric current and phase inductance. At certain speed, known as the base speed, the back EMF becomes the predominant term in the voltage equation (Eq. (1)), and then, the produced torque must be controlled by adjusting the θ_{on} and θ_{off} angles. In Eq. (1), V_{DC}, R, i, ω, and $L(\theta, i)$ are the source voltage, the phase resistance, the phase electric current, the rotor angular speed and the angular position, and electric current dependent phase inductance, respectively.

$$V_{DC} = Ri + L(\theta, i)\frac{di}{dt} + i\omega\frac{dL(\theta, i)}{d\theta} \tag{1}$$

2. Torque production in switched reluctance machines

The SRM motion is directly linked to the minimum reluctance principle, that is, when the stator pole winding is energized, the closest rotor pole tends to move toward the energized stator pole, and during this process, the reluctance is minimized and the inductance is maximized. The coordination of this process leads to rotational acceleration. The electromagnetic torque produced by an SRM phase may be expressed as in Eq. (2), where T_e is the electromagnetic torque.

$$T_e = \frac{1}{2}i^2\frac{\partial L(i, \theta)}{\partial \theta} \tag{2}$$

From Eq. (2), one can infer that: (1) the torque production does not depend on the direction of the electric current because of their quadratic relation; (2) the direction of the torque produced depends exclusively on the inductance derivative according to the rotor position. The inductance depends on the electric current and on the rotor position; and (3) the SRM is able to operate in all four torque-speed quadrants [19].

The total instantaneous torque produced by the SRM can be expressed as the sum of the individual torque produced by the phases as in Eq. (3), where N is the number of phases and $T_{e,k}$ is the electromagnetic torque produced by the phase k. Each phase torque can be calculated as Eq. (2).

$$T_{tot} = \sum_{k=1}^{N} T_{e,k} \tag{3}$$

Thus, the average developed torque $(\overline{T_{tot}})$ in a period is given by the time integral of the total torque produced in the same period as in Eq. (4), where τ is one revolution period.

$$\overline{T_{tot}} = \frac{1}{\tau}\int_{0}^{\tau} T_{tot}dt \tag{4}$$

As aforementioned, due to the SRM working principle and driving methods, strong torque undulations occur. These undulations are known as torque ripples and one way of measuring this phenomenon is through the ratio between peak to peak torque and the average torque produced in one cycle as in Eq. (5), where $\max(T_e)$ and $\min(T_e)$ are the maximum and minimum torque produced in one electric period, respectively.

$$T_{ripple} = \frac{\max(T_e) - \min(T_e)}{\overline{T_{tot}}}$$

(5)

3. Average torque control

The main aspect of average torque control (ATC) techniques is to keep a constant value of reference current throughout an electric cycle. Therefore, the major task of the controller is to adjust the control variables, for instance driving angles (θ_{on} and θ_{off}) and electric current reference (i^*), for each operation point (T, ω) in the torque-speed plane. The basic structure for ATC is presented in **Figure 4**.

There are two main methods for implementing the ATC [20]. The first consists of maintaining the driving angles while varying the electric current reference in each cycle, and the realization of this method is straightforward, but the operation region is limited and no efficiency optimization may be achieved. In the second method, both the electric current and the driving angles are controlled. Thus, although the control system becomes more complex and expensive, a good performance can be achieved, and the machine can operate in the entire speed range.

Studies focus on methods that enable real time variation of all control variables. This can be achieved online, through formulation and controllers or through genetic algorithms, or it can be achieved offline, using lookup tables [20, 21].

There are different combinations of control variables that attain the same control requirements for each operation point, such as minimizing the torque. It is possible, through cumbersome simulations, to create lookup tables containing the optimum values for each of these parameters according to the control objective.

Different optimization objectives may be conflicting, for example, minimizing torque ripple and maximizing efficiency. Thus, for a multi-objective optimization, a weighting process must be added to the optimization [22]. In this chapter, only torque ripple minimization is considered as objective.

Therefore, for the tables, creation diverse simulations were realized with the SRM modeling process developed in [23]. An open loop simulation of the system is implemented, while the control parameters and the load torque are varied covering all the operation region of the SRM (One Factor at a Time – OFAT optimization).
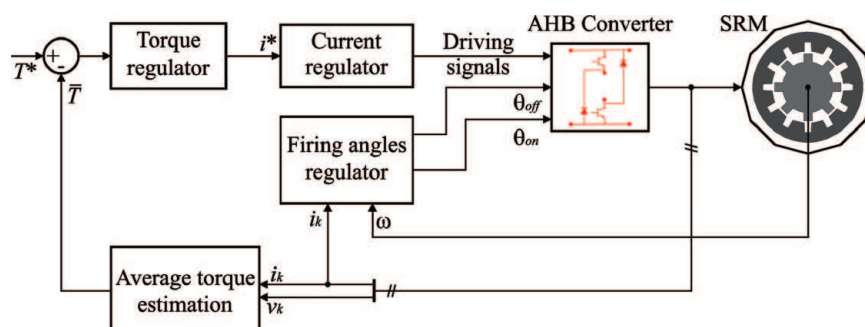
Figure 4.
Closed-loop average torque control.

After each simulation, the data are stored. The stored data incorporate the steady state rotational speed, the control variables used, and the torque ripple. By comparing the data, a combination of control parameters is selected, which enable the SRM to operate in the entire torque × speed plane (T, ω) with the minimum torque ripple. The selected parameters are stored in a lookup table.
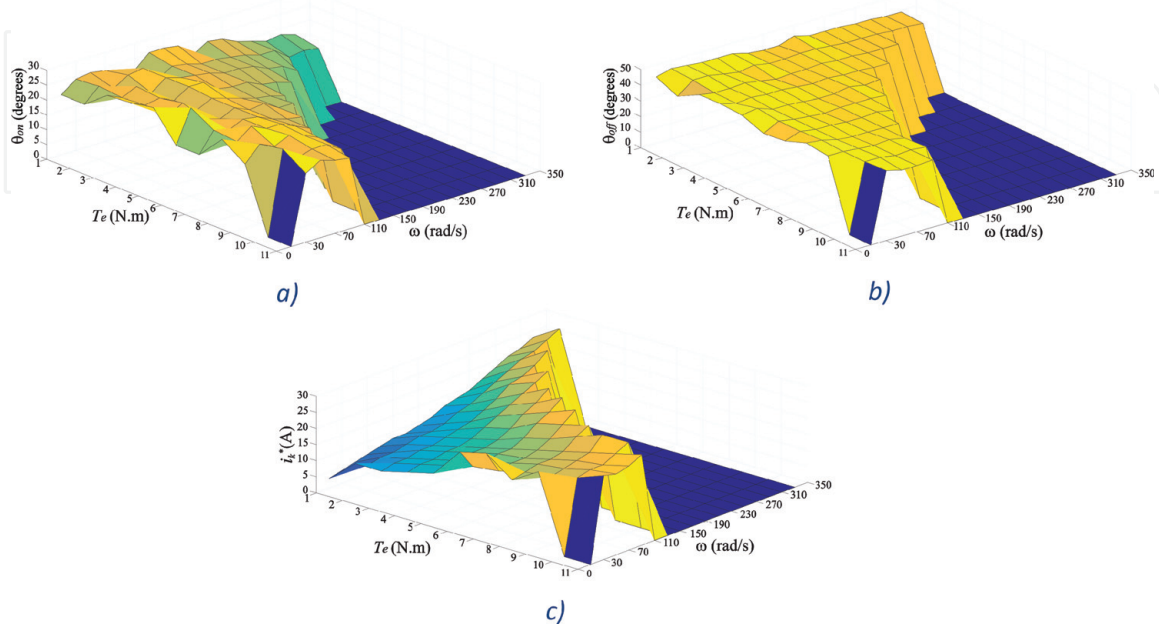
Graphic representation of the lookup tables with the optimum values for the turn-on angle, turn-off angle, and reference current from the simulations are presented in **Figure 5**. As expected, both the turn-on and the turn-off angles must be advanced according to the rotational speed and load torque rise. On the other hand, the optimal electric current rises according to the increase in speed and load torque.

In some applications, the excitation voltage must also be considered as control parameter. The addition of one control parameter increases exponentially the number of simulations. To avoid this problem, Inderka [20] proposed a closed-loop average torque control method known as direct average torque control (DATC). The method is based on comparing the reference torque to the average torque produced. However, measuring the average torque with a torque transducer is expensive. To overcome this downside, the average torque may be estimated through the machine terminal quantities.

3.1 Average torque estimation

Considering SRMs with two or more phases, two phases may contribute to torque generation during commutation. Thus, the average torque estimation becomes dependent on the flux linkage derivative estimation, which may be calculated with terminal quantities, that is, phase current and phase voltage.

The torque production principle in SRM is similar to the torque production principle of solenoids. Assuming that the mechanical work incremented in a period is proportional to the rate of change in coenergy [6], the mechanical energy (W_{mec}) can be expressed as in Eq. (6), where $\phi(\theta, i)$ is the angular position and phase current dependent flux linkage. With this equation, the average torque $(\overline{T})$ can be calculated as a function of the number of phases (N_k) and number of rotor poles (N_r), as in Eq. (7). Also, Eq. (1) can be rearranged to express the flux derivative (Eq. (8)).

Figure 5.
Graphic representation of the lookup tables with the optimum control parameters values for torque ripple minimization: (a) $\theta_{on}(\omega, T)$, (b) $\theta_{off}(\omega, T)$, and (c) $i_k^*(\omega, T)$.

$$W_{mec} = \oint i \frac{d\phi(\theta, i)}{dt} dt \qquad (6)$$

$$\overline{T} = \frac{N_k N_r}{2\pi} W_{mec} \qquad (7)$$

$$\frac{d\Phi(\theta, i)}{dt} = V_{DC} - Ri \qquad (8)$$

The average value of torque produced by the phases does not differ much from one another in each cycle due to phase symmetry, thus enabling to use only one average torque estimator. Note that in practice, the use of only one torque estimator reduces the cost of the project, but also can decrease the speed and quality of the controller. **Figure 6(a)** depicts the structure used to estimate the average torque of one SRM phase according to Eqs. (6)–(8). Only the current and voltage quantities are required. For implementation, it is not necessary to calculate the derivative of flux, since it is given by the difference between the excitation voltage and the resistance voltage drop. Note that the integrator must be reset every time the current returns to zero in order to avoid the drifting problem during practical implementation. Also, the sample and hold logic must be used to hold the mechanical energy value at the instant the current reaches zero. **Figure 6(b)** presents the waveform of the quantities used to estimate the average torque produced in one cycle.

3.2 Direct average torque control

In total, the DATC method relies on three lookup tables, one for reference electric current of the phase $i_k^*(T, \omega)$, one for the turn-on angle $\theta_{on}(T, \omega)$, and one for the turn-off angle $\theta_{off}(T, \omega)$. The block diagram structure for the DATC is presented in **Figure 7**. An external speed loop is responsible to generate the reference torque through a PI controller. A feedforward is added to the control system and generates a new reference torque. The lookup tables output the control parameter values. A hysteresis current regulator drives the AHB converter according to the control parameters.

Since the average torque is estimated only once per electric cycle, the DATC method requires low sampling ratio. This imply in lower cost for the controller mass production. On the other hand, the controller response to reference torque variations tend to be slow. To cope with that, one can use a torque estimator per SRM phase and recalculate the average torque at the beginning of each phase electric cycle. This solution increases the computational effort and cost of the system.

In order to verify the method, a computational model was developed in Matlab/Simulink® environment. The mathematical model of the SRM was developed as
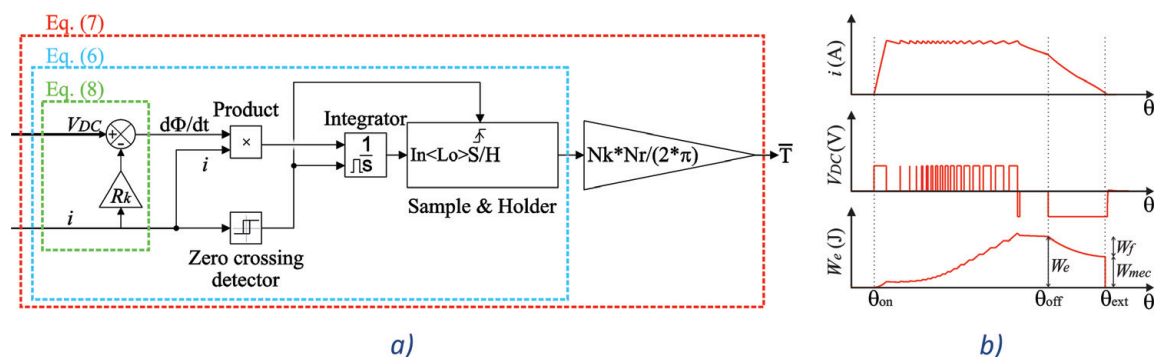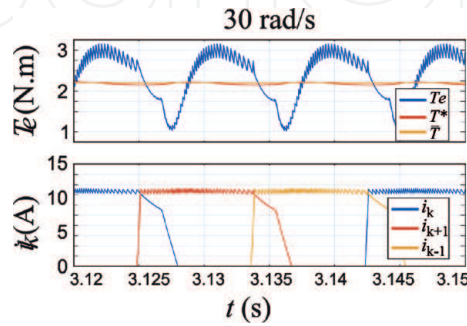

Figure 6.
Average torque estimation: (a) structure based on aforementioned equations; (b) time domain representation used in the mechanical energy estimation.
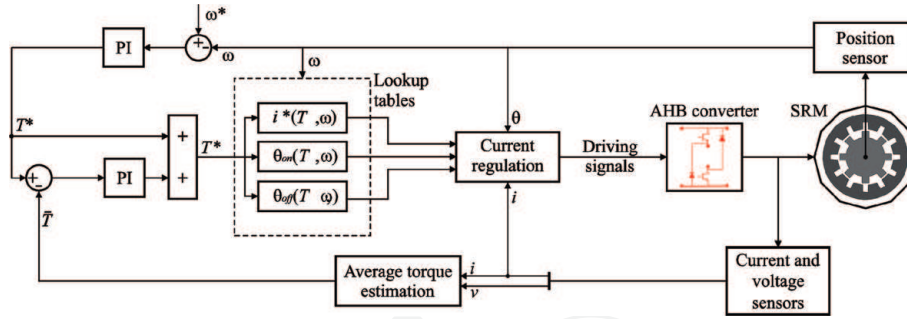
Figure 7.
*Block diagram for the direct average torque control.*

Figure 8.
DATC simulation results for setup S_1.

explained in [23]. The parameters for the SRM used for the simulation tests are presented in Appendix A. The base speed of the SRM is 954.93 *rpm* or 96 *rad/s*. The excitation voltage for the tests was maintained in 80 *V*. A constant load torque of 2 *N.m* was used for the tests.

For this test and for the following tests, two types of simulation are performed. The first simulation ($S1$) is performed for a constant load of 2 *N.m* and a reference speed of 30 *rad/s* (below base speed). For the second simulation ($S2$), the load is maintained in 2 *N.m* and the reference speed is increased to 130 *rad/s* (above base speed). The same simulations setup will be used in future subsections for the other torque control methods presented, where they will be referred to as $S1$ and $S2$, respectively.

The simulation results for the $S1$ and $S2$ setups using the DATC method are presented in **Figures 8** and **9**, respectively. The torque ripple in $S1$ conditions is 69.4%, while in $S2$ conditions, the torque ripple is 58.64%. Note that in $S1$, when the rotational speed is 30 *rad/s*, the electric current is limited by the hysteresis controller, while in $S2$, when the rotational speed is 130 *rad/s*, there is almost no chopping
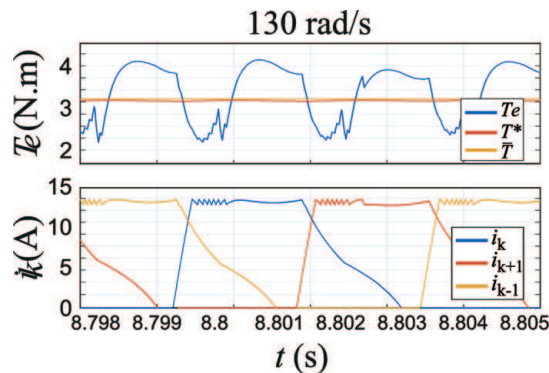
Figure 9.
DATC simulation results for setup S_2.

in the current waveform because the back EMF is high and preclude the current rise. The results show a high torque ripple in both simulation setups. This occurs because the DATC main objective is to control the average torque produced, and this way, the instantaneous torque is not controlled, leading to a high torque ripple response.

4. Instantaneous torque control

The biggest difference between ATC and instantaneous torque control (ITC) is that for the ITC methods, the electric current is regulated at every sampling period, while for ATC methods, the electric current is maintained constant through the entire excitation period. Therefore, the torque must be measured/estimated at every sampling period for ITC [24].

Another relevant factor is the operation region for each type of controller. The ATC methods may be applied through the entire speed range of operation. In contrast, the ITC methods have a shortened operation region and can only be applied while the controller is capable of controlling the current with accuracy. This becomes impractical when the speed grows above base speed because the back EMF forces the electric current in the opposite direction of the desired current.

Regarding the ITC methods, there are three main techniques present in the literature, which are the direct torque control (DTC), current profiling through torque sharing functions (TSF), and direct instantaneous torque control (DITC). Each of these techniques has its own derivations. Nonetheless, all of them depend on the instantaneous torque value. However, as in the case of the ATC, measuring the instantaneous torque may be expensive. Thus, to lower the price of the drive system, an instantaneous torque estimation technique may be employed.

4.1 Instantaneous torque estimation

Measuring the instantaneous torque is often expensive. Thus, sensorless torque estimation is preferable over torque transducer provided that the estimated torque accuracy is satisfactory.

The SRM model used in the simulations requires two lookup tables, one that returns the electric current according to flux linkage and electric current ($i(\Phi, \theta)$) and the other that returns the electromagnetic torque according to the electric current and rotor position ($T(i, \theta)$).

If the model is accurate, the torque lookup table may be used to estimate the electromagnetic torque produced by the SRM given the rotor position and the electric current in the phase winding. The electromagnetic torque estimation may also be performed using other lookup tables. For example, the electromagnetic torque may be estimated through the magnetic flux linkage and the rotor position with a $T(\Phi, \theta)$ table. This method also depends on a precise position sensor. If no position sensor may be used, the electromagnetic torque can also be estimated through the electric current and the voltage in the phase winding. With these two quantities, the flux linkage may be calculated online and used as input to a $T(i, \Phi)$ lookup table.

4.2 Current profiling technique through torque sharing functions

Given the relation between electromagnetic torque and electric current, it is possible to indirectly control the instantaneous torque produced through current control. On the other hand, the nonlinearities of the inductance profile must be

accounted. Thus, to maintain the produced torque constant, the current profile presents a nonlinear waveform that varies according to the SRM characteristics, which is hard to interpolate.

The current profiling technique consists of controlling the electric current around a desired reference. The reference current is generated aiming to minimize the torque ripple or maximize the system efficiency. Some current profiling techniques are based on finite element analysis (FEM) [3, 4], and other methods are based on generating a reference electric current from desired torque profiles named torque sharing functions (TSF). The TSF may be generated and/or compensated online or offline. The TSF are responsible for dividing the produced torque equally through the phases and may present different formats. The most common formats are linear, sinusoidal, cubic, and exponential. In some cases, modifications are applied to these TSF by performing optimization techniques with different objectives.

Considering that the controller is fully capable of regulating the electric current, the torque production may be distributed among the phases in such a way that the sum of the torque produced by the phases is equal to the reference torque (T^*).

4.2.1 Torque sharing functions

The reference torque and rotor position are used as inputs of the TSF. The TSF outputs the reference torque of each phase (T_k^*). The torque division follows the profile defined in Eq. (9), where θ_{on}, θ_{off}, θ_{al}, and θ_{ov} are the turn-on, turn-off, alignment, and overlapping angles, respectively. The functions that rule the profile while the phase is entering and leaving the commutation period are defined as $f_{up}(\theta)$ and $f_{down}(\theta)$, respectively. The TSF is divided into five sectors according to angular position.

$$T_k^*(\theta) = \begin{cases} 0, \& 0 \leq \theta \leq \theta_{on} & \text{sector 1} \\ T^* f_{up}(\theta), \& \theta_{on} \leq \theta \leq \theta_{on} + \theta_{ov} & \text{sector 2} \\ T^*, \& \theta_{on} + \theta_{ov} \leq \theta \leq \theta_{off} - \theta_{ov} & \text{sector 3} \\ T^* f_{down}(\theta), \& \theta_{off} - \theta_{ov} \leq \theta \leq \theta_{off} & \text{sector 4} \\ 0, \& \theta_{off} \leq \theta \leq \theta_{al} & \text{sector 5} \end{cases} \tag{9}$$

In the literature, there are many functions to describe the rise and descend of the reference torque during commutation. The equations referring to the most commonly found TSF are presented hereafter along with the expected waveform for these functions. In the equations, the indexes *lin*, *sin*, *cub*, and *exp* indicate the linear TSF, the sinusoidal TSF, the cubic TSF, and the exponential TSF, respectively.
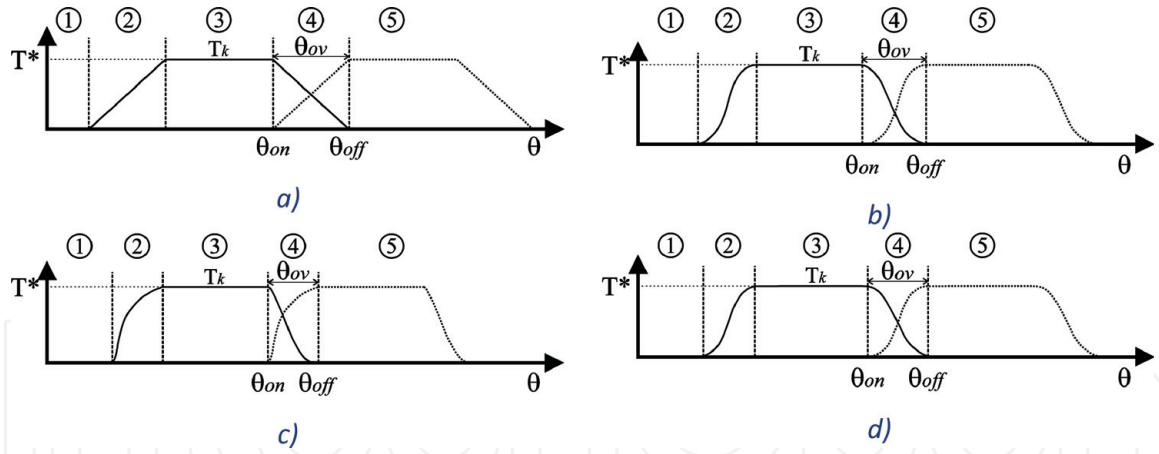
The up and down functions for the linear TSF are presented in Eqs. (10) and (11). The reference torque waveform for this TSF is presented in **Figure 10(a)**.

$$f_{up}^{lin}(\theta) = \frac{1}{\theta_{ov}}(\theta - \theta_{on}) \tag{10}$$

$$f_{down}^{lin}(\theta) = 1 - \frac{1}{\theta_{ov}}(\theta - \theta_{off}) \tag{11}$$

The equations for the sinusoidal TSF are presented following. The reference torque waveform is depicted in **Figure 10(b)**.

$$f_{up}^{sin}(\theta) = \frac{1}{2} - \frac{1}{2} \cos\left[\frac{\pi}{\theta_{ov}}(\theta - \theta_{on})\right] \tag{12}$$

Figure 10.
TSF waveforms and sector divisions: (a) linear TSF, (b) sinusoidal TSF, (c) exponential TSF, and (d) cubic TSF.

$$f_{down}^{sin}(\theta) = \frac{1}{2} + \frac{1}{2} \cos\left[\frac{\pi}{\theta_{ov}}(\theta - \theta_{off})\right] \tag{13}$$

For the exponential TSF, the up and down functions are described by Eqs. (14) and (15), respectively, and the waveform of the expected reference torque is shown in **Figure 10(c)**.

$$f_{up}^{exp}(\theta) = 1 - \exp\left(-\frac{(\theta - \theta_{on})^2}{\theta_{ov}}\right) \tag{14}$$

$$f_{down}^{exp}(\theta) = 1 - f_{down}^{exp}(\theta - \theta_{off} + \theta_{on}) \tag{15}$$

The last TSF is the cubic. The up and down functions are represented as followed in Eqs. (16) and (17), while the waveform of the reference torque is illustrated in **Figure 10(d)**.

$$f_{up}^{lin}(\theta) = \frac{1}{\theta_{ov}}(\theta - \theta_{on}) \tag{16}$$

$$f_{down}^{lin}(\theta) = 1 - \frac{1}{\theta_{ov}}(\theta - \theta_{off}) \tag{17}$$

Observing Eqs. (10)–(17), one can perceive that the firing angles play an important role on the TSF creation. Normally, these angles are kept constant throughout the operation range. Varying the firing angles enables better performance in different operation points. Thus, for this book chapter, an OFAT optimization [22] was performed, and the optimum angles for each operation point (T, ω) were stored in lookup tables. Note that the optimum firing angles for each TSF are different. Thus, two lookup tables are necessary for each TSF, totalizing eight lookup tables.

4.2.2 Current profile creation

After obtaining the reference torque signals for each phase with the TSF, the reference current signals per phase (i_k^*) must be determined. This procedure may be accomplished by inverting the $T(i, \theta)$ lookup table into an $i(T, \theta)$ lookup table. In [25], the authors use the inverted $T(i, \theta)$ LUT to estimate electromagnetic torque and compare to a non-unity torque reference. The inverted $T(i, \theta)$ LUT is also

applied in [26, 27], and in these cases, the contribution of the authors is to propose an alternative to commonly used TSFs. Alternatively, a nonlinear function of current as function of torque and rotor position can be used. The development of such function is cumbersome and requires a mathematical approach that models the inductance variation as function of electric current and rotor position. The analytical inversion function is expressed in Eq. (18), where $L_{0p}(\theta)$ is the inductance derivative for one SRM phase before saturation, that is, with low electric current, $f(\theta)$ is the function that describe the ratio change between the produced torque and the electric current according to the saturation level. More detailed explanation about the derivation of Eq. (18) may be found in [28].

The $i(T, \theta)$ lookup table obtained after inverting the $T(i, \theta)$ lookup table from the SRM model is presented in **Figure 11**. The parameters of the SRM used for the development of Eq. (18) and of the lookup table are presented in Appendix A.

$$i_k\left(T_k^*, \theta\right) = \frac{2T_k^*}{L_{0p}(\theta)}\left[\frac{f(\theta)}{2} + \sqrt{\frac{f^2(\theta)}{4} + \left(\frac{L_{0p}(\theta)}{2T_k^*}\right)^{\frac{1}{p}}}\right] \qquad (18)$$

4.2.3 Simulation results

The block diagram implemented in the Matlab/Simulink® environment is represented in **Figure 12**. The speed error is processed in a PI controller to create the reference torque (T^*), and the reference torque and the rotational speed are used as input of the optimum firing angles lookup tables. The optimum angles and the reference torque are used to create the phase reference torque (T_k^*) through the TSF. The phase reference torque is then transformed in a phase reference current. Now, a hysteresis current controller drives the AHB in order to maintain the electric current following the reference.

To verify the TSF with the best torque ripple reduction capability, simulations throughout the entire speed range of operation were done, in steps of 10 rad/s. The results are presented in **Figure 13**. In the figure, a vertical line demarks the base speed ($\omega_b = 96\ rad/s$). The presented TSF returns similar torque ripple. The higher disparity occurs at 170 rad/s, where the exponential TSF have 19.59% less torque ripple than the cubic TSF. However, since the current profiling is an ITC method, it is expected that above base speed results are not acceptable and the interest speed range lies below the base speed. Below base speed, the sinusoidal TSF and the cubic TSF convey minor torque ripple. Thus, for future comparisons, the sinusoidal TSF will be employed because of its simple implementation.
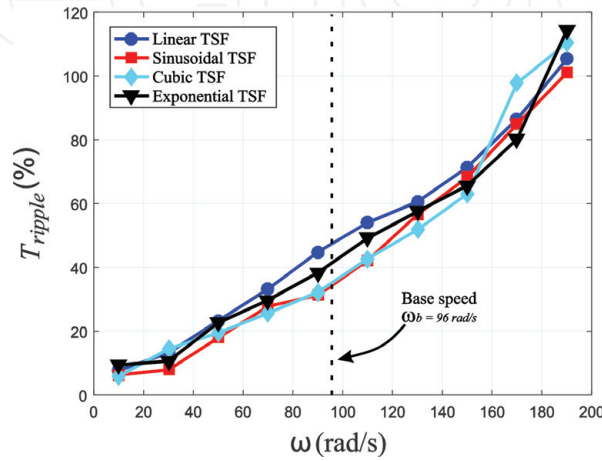
The simulation results for sinusoidal TSF are presented in the following figures. The setups used in the simulations were the Simulation 1 ($S1$) and Simulation 2 (S_2) setups. The results for S_1 and S_2 setups are presented in **Figures 14** and **15**,
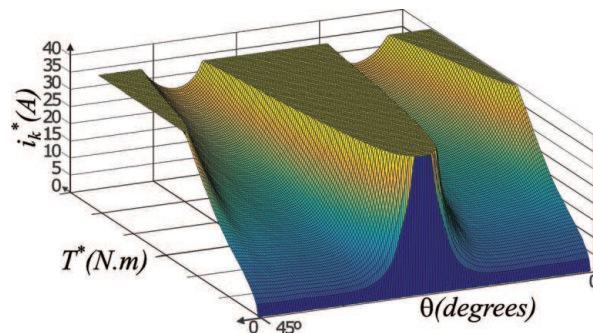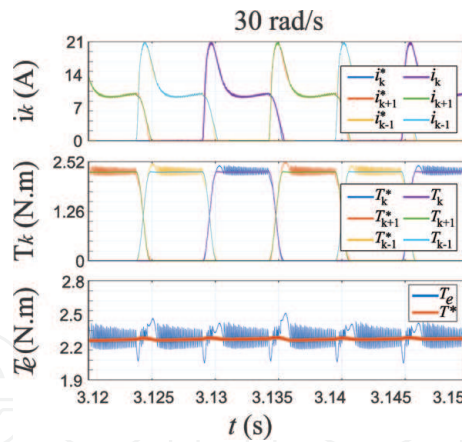

Figure 11.
$i(T, \theta)$ *lookup table.*
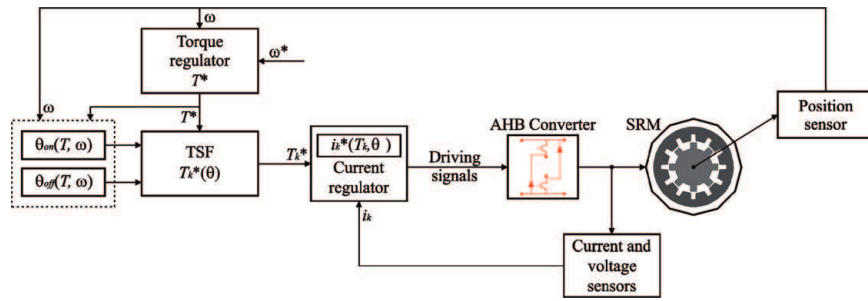
Figure 12.
Block diagram representing the current profiling through TSF with optimal driving angles.
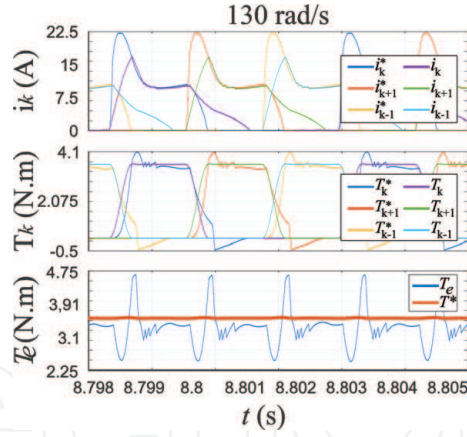

Figure 13.
Torque ripple level for each of the presented TSF in different speeds.

Figure 14.
Current profiling through sinusoidal TSF simulation results for setup S_1.

respectively. With S_1 setup, the current is accurately profiled, and the torque ripple is diminished, however, in S_2, the back EMF is high, and the controller is not capable of profiling the current, thus the torque ripple is considerably higher. The torque ripple, turn-on angle, and turn-off angle for each TSF using both setups are presented in **Table 1**.

When the speed rises, the error between reference torque and instantaneous torque produced by each phase rises as well. This phenomenon occurs for every TSF because there is a small error between the instantaneous current and the current reference at the phase energization and at the phase demagnetization. This current error is a consequence of the reduced maximum increase and decrease ratio of the electric current. When the speed rises, the back EMF also rises, diminishing the

Figure 15.
Current profiling through sinusoidal TSF simulation results for setup S_2.

	Turn-on angle (°)		Turn-off angle (°)		Torque ripple (%)	
TSF	S_1	S_2	S_1	S_2	S_1	S_2
Linear	25.6	23.0	43.4	42.5	13.21	60.26
Sinusoidal	25.3	23.5	43.5	42.5	7.92	55.87
Exponential	27.3	23.6	43.5	43.0	10.7	58.12
Cubic	26.0	23.9	43.5	43.8	14.52	53.24

Table 1.
Control parameters for the different TSF using S_1 and S_2 setups.

maximum current change ratio. Then, the current error is reflected in the electromagnetic torque produced, causing the torque ripple to rise.

4.3 Direct torque control

The direct control technique (DTC) for SRM is based on the DTC technique for induction machines from the 80s and present simple dynamic and robustness. The DTC may be adapted to SRMs with any number of phases. However, three or five phases' adaptations are more recurrent in the literature than four phases' adaptations. This technique does not control the electric current, and instead, it aims to control the torque directly by applying different voltage states to the phases. The voltage states are stored in vectors and are chosen according to torque and magnetic flux linkage errors [29, 30].

The DTC uses flux linkage and electromagnetic torque values as control variables. The torque and flux conditions are used to determine which voltage state vector should be applied to the AHB in order to control the instantaneous torque produced. Therefore, to better understand the working principle of this method, the relation between excitation voltage and flux linkage and how the produced torque can be controlled through magnetic flux linkage changes must be clarified.

The vector of magnetic flux linkage in the stator ($\vec{\lambda_s}$) may be calculated as the time integral of the difference between the excitation voltage ($\vec{V_{DC}}$) and the voltage drop in the resistance ($R_s \vec{i_s}$) minus the initial flux linkage value ($\vec{\lambda_0}$), as described in Eq. (19).

$$\vec{\lambda_s} = \int_0^\tau \left(\vec{V_s} - R_s \vec{i_s} \right) dt - \vec{\lambda_0} \tag{19}$$

Generally, the voltage drop in the stator resistance is much smaller than the excitation voltage and then may be disregarded. In this case, the variation of flux linkage in the stator depends only on the voltage vector applied and can be described as in Eq. (20), indicating that a voltage vector applied to a phase causes a variation on the flux linkage of the same direction.

$$\Delta \overrightarrow{\lambda_s} = \overrightarrow{V_s} \Delta t \qquad (20)$$

To calculate the flux linkage vector in the stator, one must know the flux linkage from each SRM phase and parse them to their stationary component. For a three-phase SRM, the Clarke transform may be used to calculate the stationary components of the magnetic flux linkage vector (λ_α and λ_β) through Eqs. (21) and (22), respectively.

$$\lambda_\alpha = \lambda_a - \lambda_b \cos 60^o + \lambda_c \cos 60^o \qquad (21)$$
$$\lambda_\beta = \lambda_b \sin 60^o - \lambda_c \sin 60^o \qquad (22)$$

If the stationary components of flux linkage in the stator are know, it is possible to calculate the total flux linkage as:

$$\lambda_s = \sqrt{\lambda_\alpha^2 + \lambda_\beta^2} \qquad (23)$$

Furthermore, the stationary components may be used to estimate the rotor position through Eq. (24), enabling a position sensorless application.

$$\theta = arctan\left(\frac{\lambda_\beta}{\lambda_\alpha}\right) \qquad (24)$$

Given the relation presented above, the DTC aims to maintain the flux linkage and torque values constrained in hysteresis bands. Variations in the produced torque are similar in direction to the variations in the flux linkage vector in relation to the rotor position, hence, for a torque increase, the flux linkage vector must be advanced from the rotor position vector, while for a torque decrease, the flux linkage vector must be delayed from the rotor position vector. These flux linkage variations are named flux acceleration and flux deceleration, respectively.

4.3.1 Voltage state vectors definition

Consider a three-phase SRM 12/8 poles with an AHB as the driver converter. As mentioned in the introduction, three different voltage states may be applied to each SRM phase. Thus, the voltage state vector (U_x) has three columns and one row as: $U_x = (u_A u_B u_C)$, where u_A, u_B, and u_C are the voltage states applied to phase A, phase B, and phase C, respectively. Now, to understand the vectors creation, first, it is important to understand the voltage sector division.

In the considered SRM, the phases are spaced in 120 electric degrees as in **Figure 16**. Tracing concentric axels over the phases, three axels are obtained. Each of them may be divided into a positive part, located at the axel portion that overlap the phase, and a negative part, on the other half of the axel, for example, for phase A, we obtain the A^+ portion and the A^- portion. The axels divide the vector space in *six* sectors of 60° each, named S_0, S_1, S_2, S_3, S_4, and S_5 as observed in **Figure 16**.

It is possible to define the state vectors for the DTC from the sectors. In total, since it is possible to apply 3 different voltage states per phase and there are 3
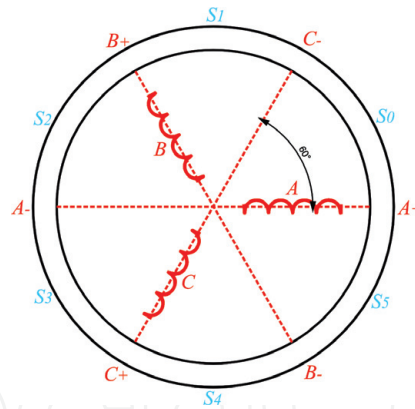
Figure 16.
*Sectors division for a three-phase SRM.*

phases, there are 27 possible state combinations. However, some of the combinations must be avoided, such as keep the three phases turned on at the same time, remaining only six combinations of interest for this case. Each of the remaining vectors are located at the center of each sector and are named U_0, U_1, U_2, U_3, U_4, and U_5 as in **Figure 17**. Each vector has three coordinates that represent the relation between the vector position and the axel portion of each phase, for example, the vector U_0 is located at the center of the sector S_0. The sector S_0 is bounded by the positive portion of axel A (A^+) and by the negative portion of axel C (C^-) and is not bounded by any portion of axel B, hence, U_0 is defined as $(1, 0, -1)$.

Table 2 summarizes the voltage states applied to the SRM phase windings according to the vector. Note that in **Figure 17**, there are two circles, one more internal and one more external. These circumferences represent the inferior and superior hysteresis bands for the flux linkage, respectively. The flux linkage vector in the stator must be maintained within this bandwidth through the application of the state vectors.

The choice of which vector must be applied depends on two conditions, one regarding the error between the reference torque and the instantaneous torque and other regarding the error between reference flux linkage and instantaneous flux linkage in the stator. Both conditions are implemented employing hysteresis

Vector	U_0	U_1	U_2	U_3	U_4	U_5
States	$(1, 0, -1)$	$(0, 1, -1)$	$(-1, 1, 0)$	$(-1, 0, 1)$	$(0, -1, 1)$	$(1, -1, 0)$

Table 2.
*Voltage vectors to be applied in the AHB converter.*
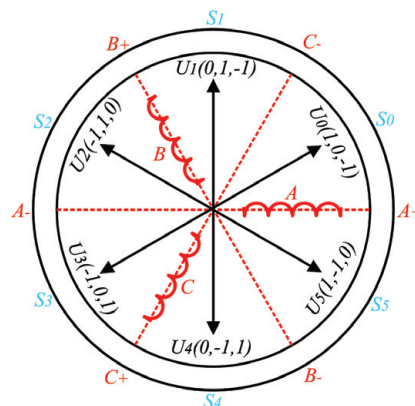
Figure 17.
Voltage state vectors definition for the DTC method.

controllers. The flux hysteresis controller receives the flux error and indicates if it necessary to increase or decrease the flux magnitude, while the torque hysteresis controller receives the torque error and indicates whether the flux vector must be accelerated or decelerated in order to control the torque production. The voltage vectors applied to make the stator flux linkage vector complete one clockwise cycle are detailed in **Figure 18** (considering that it is necessary to raise the torque). In case it is necessary to reduce the electromagnetic torque, the stator flux linkage must be rotated counterclockwise.

Table 3 compiles the logic behind the voltage state vector choice according to the sector (stator flux linkage vector position) and to the torque and flux conditions. For better understanding, considering the case in which the flux linkage vector is located at the S_4 sector, it is demanded to escalate the torque (instantaneous torque reached the inferior hysteresis band) and to reduce flux linkage (stator flux linkage reached the superior hysteresis band, that is, the external circle of **Figure 18**). In such case, the vector U_0 must be applied in order to keep the acceleration of the flux vector (increase torque) and lessen the amplitude (decrease flux), as depicted in **Figure 18**.

4.3.2 Variable magnetic flux linkage reference

The DTC requires a flux linkage reference for the hysteresis control realization. In the literature, diverse researches apply a constant reference throughout the entire operation speed range [29, 30]. However, observing the characteristics of the SRM, it is perceptible that for high values of speed (above base speed), where a high
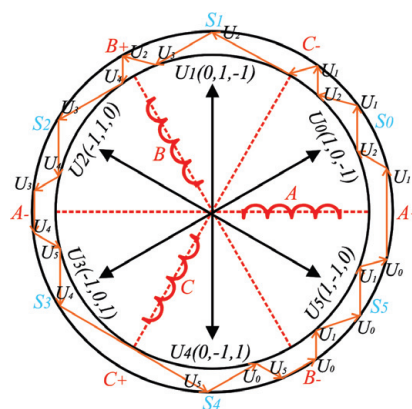
Figure 18.
State vectors defined and representation of a complete cycle of the flux linkage in the stator for a three-phase SRM.

		$T\&\lambda$ condition			
Sector	**Angular position**	$\lambda\uparrow T\uparrow$	$\lambda\uparrow T\uparrow$	$\lambda\uparrow T\uparrow$	$\lambda\uparrow T\uparrow$
S_0	$0-60^o$	$U_1(0,1,-1)$	$U_5(1,-1,0)$	$U_2(-1,1,0)$	$U_4(0,-1,1)$
S_1	$60-120^o$	$U_2(-1,1,0)$	$U_0(1,0,-1)$	$U_3(-1,0,1)$	$U_5(1,-1,0)$
S_2	$120-180^o$	$U_3(-1,0,1)$	$U_1(0,1,-1)$	$U_4(0,-1,1)$	$U_0(1,0,-1)$
S_3	$180-240^o$	$U_4(0,-1,1)$	$U_2(-1,1,0)$	$U_5(1,0,-1)$	$U_1(0,1,-1)$
S_4	$240-300^o$	$U_5(0,1,-1)$	$U_3(-1,0,1)$	$U_0(1,0,-1)$	$U_2(-1,1,0)$
S_5	$300-360^o$	$U_0(1,0,-1)$	$U_4(0,-1,1)$	$U_1(0,1,-1)$	$U_3(-1,0,1)$

Table 3.
DTC switching table for an three-phase SRM.

electric current is required, the flux linkage behavior becomes nonlinear according to the saturation level causing the torque ripple to increase according to the rotational speed increase. To overcome this drawback, a variable flux linkage reference may be used.

In certain operation speed, the electromagnetic torque developed starts to present drops, causing the torque ripple growth according to speed. This speed is defined as the critical speed (ω_{crit}). To estimate the critical speed, an open loop simulation with constant operation speed must be performed while observing the electromagnetic torque waveform. According to the speed rise, it is possible to note dips in the instantaneous torque waveform [29]. For the SRM used in this book chapter studies, the critical speed (ω_{crit}) is approximately 37.5 rad/s.

The flux linkage reference used here is divided into three cases, one for speeds below the critical speed, the second for speeds between the critical and the base speed, and the third for speeds above the base speed. For the first case, the flux reference is obtained with a PI controller that processes the speed error. For the second case, a function that describes the optimum flux decaying according to the speed increase is implemented ($\lambda_{dec}(\omega)$). In the third case, the flux linkage reference is maintained constant at the nominal value.

The decaying flux linkage function is established using an OFAT optimization to find the optimum flux linkage values for each operation speed. Then, the optimum values are interpolated to create the $\lambda_{dec}(\theta)$ function. The function is a sum of sinusoids presented in Eq. (25). The coefficients used in the equation are displayed in **Table 4**.

$$\lambda_{\text{dec}}(\omega) = \sum_{i=1}^{4} A_i \sin\left(B_i \omega + C_i\right) \qquad (25)$$

Thus, the flux linkage reference ($\lambda^*(\omega)$) for the entire speed range of the DTC operation is described as following:

$$\lambda^*(\omega) = \begin{cases} PI controller output,\, 0 \leq \omega < \omega_{crit} \\ \lambda_{dec}(\omega),\, \omega_{crit} \leq \omega < \omega_b \\ 0.0875,\, \omega_b \leq \omega \end{cases} \qquad (26)$$

4.3.3 Simulation results

The block diagram for the DTC implementation is shown in **Figure 19**. The error between reference and instantaneous speed is processed through a PI controller to generate the reference torque. The flux linkage reference is according to Eq. (26). The torque reference is compared to the instantaneous torque, and the error is processed by a hysteresis controller to determine the torque condition. The same happens for the flux linkage to return the flux condition. Clarke transform is employed to estimate position and to calculate the total flux linkage in the stator. The sector selector block informs the sector according to the estimated position. The

Coefficients	A_1	B_1	C_1	A_2	B_2	C_2
Values	0.128	0.02826	−0.4405	0.04907	0.06595	−0.02546
Coefficients	A_3	B_3	C_3	A_4	B_4	C_4
Values	0.01876	0.1314	−1.89	0.01024	0.01658	4.76

Table 4.
A_i, B_i, C_i, and D_i coefficients for the $\lambda_{dec}(\theta)$ function.
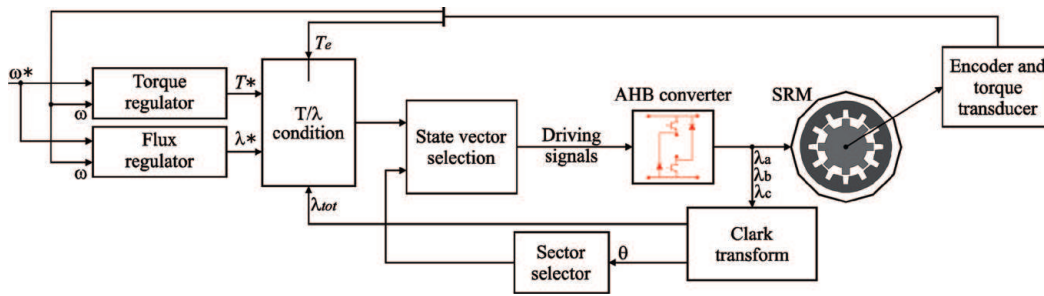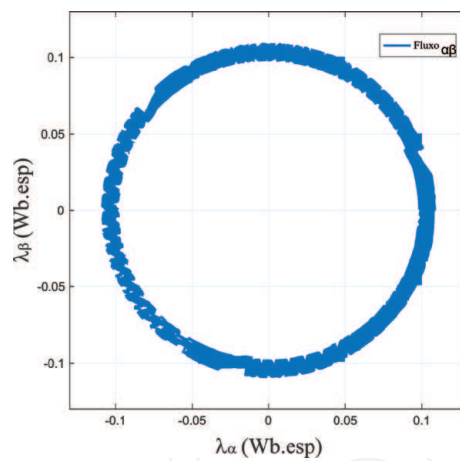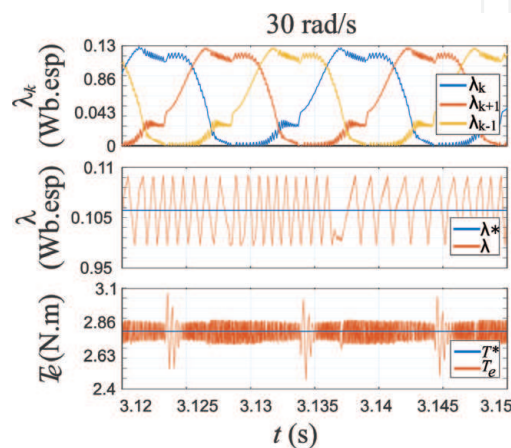
Figure 19.
Block diagram of the DTC.

sector and the conditions are then used to choose the voltage state vector according to **Table 3**.

The DTC controls the electromagnetic torque produced and the flux linkage in the stator. Considering the stationary frame ($\alpha\beta$-reference frame), the phase of the flux linkage vector must be accelerated or decelerated to produce torque, while the magnitude of the vector must be maintained constant. Plotting the α flux component (λ_α) against the β flux component (λ_β) should result in a circular profile as depicted in **Figure 20**.
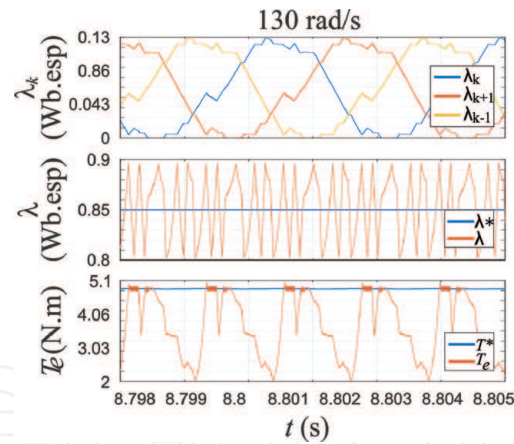
The results obtained using the DTC with the S_1 and S_2 conditions are presented in **Figures 21** and **22**, respectively. The figures contain the waveforms of the flux linkage of each phase, instantaneous and reference magnitude of the flux linkage in

Figure 20.
Flux linkage in stationary coordinates for the DTC.

Figure 21.
DTC simulation results for setup S_1.

Figure 22.
DTC simulation results for setup S_2.

the stator (in stationary frame), and the instantaneous and reference electromagnetic torque. The torque ripple returned in both conditions is 24.41%, for the S_1 simulation, and 72.84%, for the S_2 simulation.

4.4 Direct instantaneous torque control

The direct instantaneous torque control (DITC) was first envisioned by Inderka [31]. The closed-loop control system uses a combination of double band current hysteresis controllers to generate the driving signals for each SRM phase. Differently from the current profiling through TSF, the DITC controls the torque directly.

The method dynamically divides the torque between two phases during commutation. The control system coordinates the AHB switch states according to an enabled conduction condition signal and to the instantaneous torque produced by each phase.

For better understanding of the DITC, first, some concepts must be clarified. In **Figure 23**, the electric currents for the three SRM phases are depicted. Two different intervals may be defined. One is the commutation interval, defined as the period in which two phases are simultaneously in conduction and both phases are responsible for the torque production. The other one is the single conduction interval, defined as the period in which only one phase is in conduction and is responsible for the entire torque production.

Furthermore, during the commutation interval, the two phases in conduction may be defined as incoming phase and outgoing phase. The outgoing phase is the
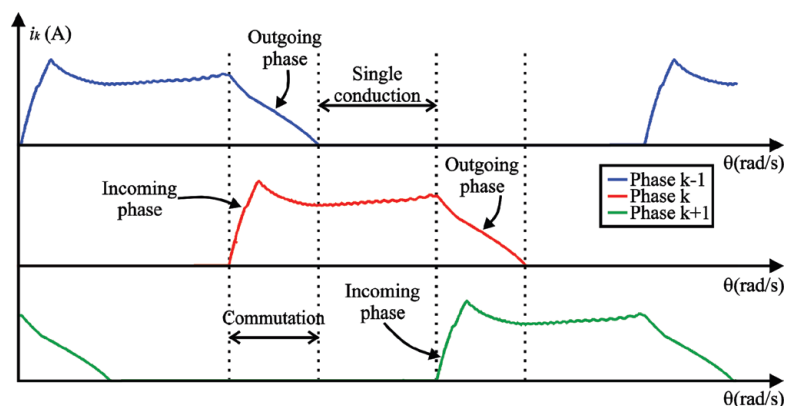
Figure 23.
Electric current in phases when DITC is applied and concepts definition.

phase that is in the end of the conduction period and is leaving commutation, while the incoming phase is the phase that is entering the conduction period.

The DITC classifies the phases, indicating whether the phase is enabled to enter conduction. The phase position must be in the interval between the turn-on angle and the turn-off angle ($\theta_{on} \leq \theta \leq \theta_{off}$) to be considered enabled to enter conduction. If this condition is satisfied by only one phase, single conduction is characterized, and the control system changes the voltage state of this phase to control the torque produced. If two phases satisfy the condition, phase commutation is characterized, and the voltage states of both phases must be individually controlled in such way that the sum of the produced torque by the phases equals to the total reference torque. The control strategies used in both cases are minutely explained hereafter.

4.4.1 State machines for direct instantaneous torque control

During commutation, there are two independent control logics simultaneously implemented. One for the incoming phase and one for the outgoing phase. The incoming phase is preferred for the torque production because the outgoing phase has already started the demagnetization process. Thus, the outgoing phase must be energized only if the incoming phase is not capable of producing the required reference torque by itself.

The following three state machines elucidate the working principles of DITC. The state machine in **Figure 24(a)** regulates the operation of the incoming phase, and the state machine in **Figure 24(b)** regulates the operation for the outgoing phase during commutation. Also, any phase that is in single conduction mode follows the logic within the state machine in **Figure 24(c)**. The conditions for voltage state change are indicated in the state machines, where T_{err} is the error between instantaneous phase torque and reference phase torque, *thss* is the superior torque limit, *thsm* is the superior medium torque limit, *thim* is the inferior medium torque limit, and *thii* is the inferior torque limit.

The waveforms of the total torque produced are presented in **Figure 25** along with the current of two commutating phases. In the figure, two regions are indicated during phase commutation. In region (1), the electromagnetic torque produced reaches the external inferior limit (*thii*), and then, the outgoing phase, which was in free-wheeling, is magnetized to augment the torque production, when the torque reaches back the *thim* limit, the phase state goes back to free-wheeling. In region (2), the torque reaches the superior torque band *thss*, thus the outgoing phase is demagnetized to reduce the torque production, and when the torque reaches back the *thsm* limit, the phase enter the free-wheeling state again.

Table 5 summarizes the working principle of the implemented CDTI. In this table, the voltage states (1, 0, and −1) are used to indicate the action. The "-" signal in the cells indicate that the phase is not accounted for torque production. The switching rules in **Table 5** guarantee three conditions aiming to achieve low torque ripple:
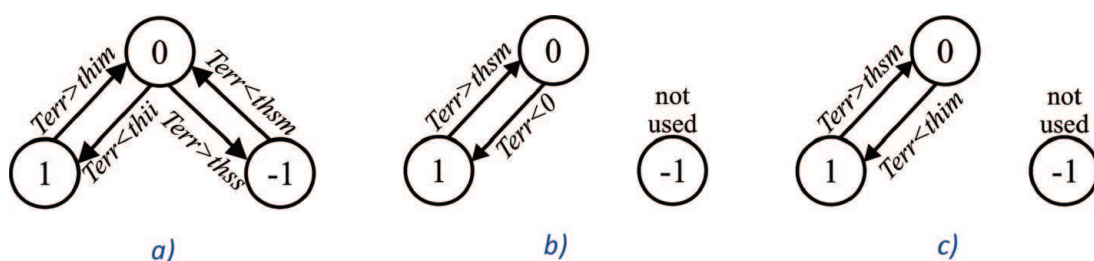
Figure 24.
State machines used in the DITC: (a) outgoing phase, (b) incoming phase, and (c) single conduction phase.
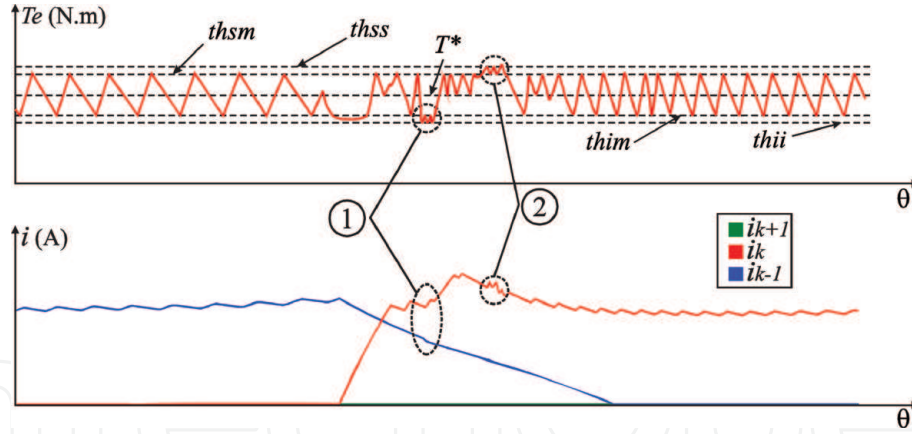
Figure 25.
Instantaneous electromagnetic torque and phase current waveforms highlighting the DITC logic.

| Phase condition			State applied to phase		
$k-1$	k	$k+1$	$k-1$	k	$k+1$
0	0	0	—	—	—
1	0	0	1|0	—	—
1	1	0	1|0|−1	1|0	—
0	1	0	−1|−	1|0	—
0	1	1	—	1|0|−1	1|0
0	0	1	—	−1|−	1|0

Table 5.
Switch voltage state logic for DITC in a three-phase SRM.

- Avoid hard-chopping to minimize switching losses and reduce the torque ripple;

- Prioritize the incoming phase for the torque production so that the electric current flowing in the outgoing phase reaches zero before the inductance profile inclination becomes negative, thus avoiding negative torque production;

- Keep the incoming phase and the single conduction phase in the free-wheeling state for as long as possible to diminish the copper losses and the torque ripple.
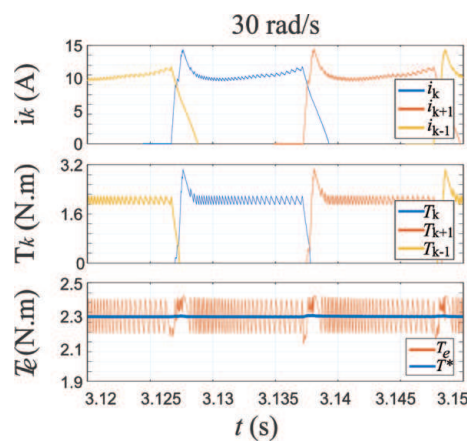
4.4.2 Simulation results

The simulated system with DITC is depicted in **Figure 26**. The speed error is processed through a PI controller to return the reference torque. The reference torque is compared to the total instantaneous torque produced. The output error is used to decide the voltage state applied to the phase according to the switching state machines. The logic used depends on a condition signal generated for each phase separately. To synthesize the phase condition, the rotor position and the firing angles are required. The firing angles used are provided by a lookup table and depend on the SRM operation point (T, ω) as for the previous methods introduced.
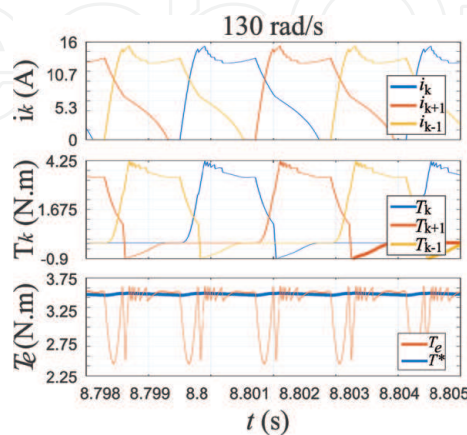
The results obtained for the DITC in S_1 and S_2 conditions are presented in **Figures 27** and **28**, respectively. The waveforms presented are the electric current
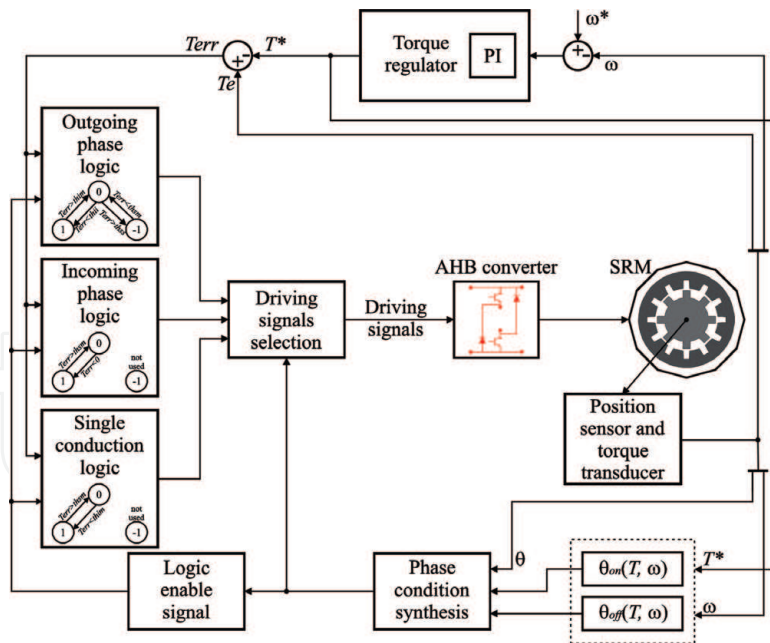
Figure 26.
Block diagram for the DITC.

Figure 27.
DITC simulation result for setup S_1.

Figure 28.
DITC simulation result for setup S_2.

in the phases, individual electromagnetic torque produced by each phase, and the instantaneous and reference total electromagnetic torque produced. The turn-on angle, turn-off angle, and torque ripple for both simulations are disclosed in

| Simulation	Turn-on angle (°)	Turn-off angle (°)	Torque ripple (%)
S_1	25.7	43.9	10.43
S_2	23.2	40.5	59.43

Table 6.
DITC simulation results for S_1 and S_2 conditions.

Table 6. When the speed is higher than the base speed, the current enters in the negative torque generation zone and causes torque dips as observed in **Figure 28**.

5. Results and discussion

For a better comparison of the methods behavior and performance throughout the SRM speed range of operation, simulations are performed from 10 *rad/s* up to the maximum possible speed with each method (even above nominal speed) at every 20 *rad/s*. The ripple factor at each speed for all methods presented in this chapter is calculated through Eq. (5), and the results are stored. The obtained values are grouped in **Figure 29** along with the results for the case where only a simple speed control is employed. The base speed (ω_b) is indicated as a vertical dashed line. The base speed for the studied machine is approximately 96 *rad/s*.

Remark that the ITC methods present better performance than the ATC method only when the electric current may be accurately controlled. Above 150 *rad/s*, the DATC presents better torque regulation capability, while below this speed, the DITC returned smaller torque ripple. Note that, below 30 *rad/s*, the current profiling with the sinusoidal TSF presented the lowest torque ripple; however, in all other speeds, the DITC surpassed the current profiling.
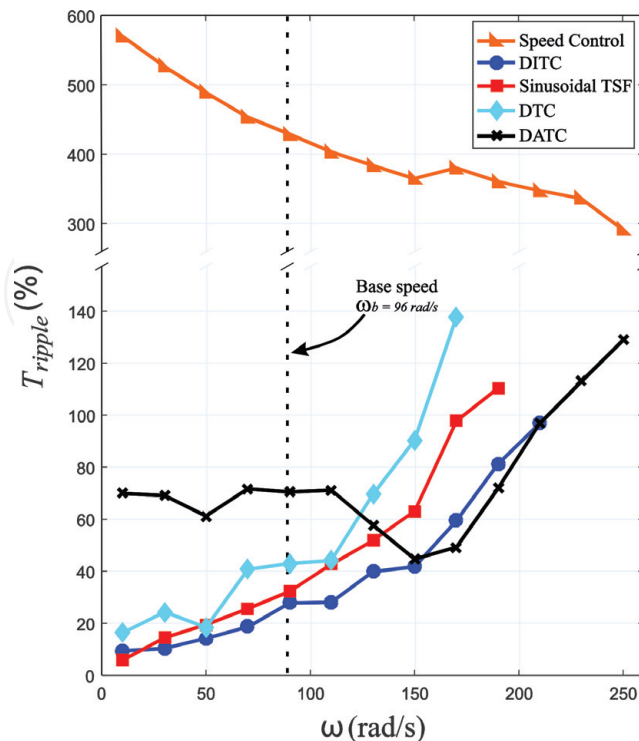
Figure 29.
Electromagnetic torque ripple for the different control methods presented throughout the entire SRM speed rage of operation.

When no torque ripple suppression method is applied, the ripple level reaches up to 570.1% at the low speed of 10 rad/s. According to the speed growth, the ripple is naturally diminished as an effect of the inertia moment. Note that, when any torque control method is employed, the torque ripple is diminished.

The preferred TSF among the studied functions are the sinusoidal one because of its easy implementation and good performance in the operation speed range of interest. When the sinusoidal TSF is compared to the other methods, it has better performance in a narrow speed range (below 30 rad/s) and then it is surpassed by the DITC. The DITC is the fittest ITC method since it naturally divides the torque production among phases and directly controls the total torque produced by the phases. However, as an ITC method, the DITC malfunctions in high speeds (above base speed), that is, torque dips appear as the speed increases until the instantaneous torque is no longer controlled. At above base speeds, the DATC method is preferred, because it considers only the average torque as target variable of the control.

6. Conclusions

In this chapter, different torque control methods were presented aiming to clarify which method is preferred for each operation point of the machine. One ATC method entitled DATC was presented, along with different ITC methods. The ITC methods addressed were the direct torque control (DTC), the current profiling through torque sharing function (TSF), and the direct instantaneous torque control (DITC). The most common TSF were used for the comparison, which are the linear, sinusoidal, exponential, and cubic TSF.

Simulations with each method were performed throughout the entire SRM speed range of operation. The DITC is the method that returned better torque ripple minimization capabilities bellow base speed, while above base speed, the DATC was the fittest method. With the presented simulations, the reader is able to understand how the SRM behavior changes according to the control method employed and operation point.

Some modifications and/or adaptations may be applied to the methods in order to improve the performance of the control system toward the chosen objective. For instance, the DATC method uses three LUT, which may be optimized according to the application and control objective. This feature makes this method very flexible.

The current profiling through torque sharing functions may be improved by creating torque profiles that account the difference between magnetization and demagnetization dynamics and how much each phase contributes to total torque produced. The DTC method can be improved by augmenting the number of sectors considered in the control strategy. The DITC technique may be modified by inserting variable turn-on and turn-off angles that can be optimized for different control objectives, such as minimize torque ripple, maximize efficiency or minimize acoustic noise, which also makes this method deeply adaptable.

Acknowledgements

Appendix: switched reluctance motor parameters

This appendix presents the parameters of the SRM used in this chapter.

- Nominal power: 1.5 kW;

- Nominal speed: 1500 rpm;

- Number of poles: 12/8 (stator/rotor);

- Operation voltage: $30 - 80$ V;

- Winding resistance: 0.3 Ω;

- Maximum flux linkage: 0.22 $Wb.esp$;

- Inertia moment (obtained through deceleration test): 0.002 kgm^2;

- Minimum phase inductance: 1.675 mH;

- Maximum phase inductance: 13.88 mH.

Author details

Marcelo Vinícius de Paula[1]*, Tárcio André dos Santos Barros[1] and Pedro José Dos Santos Neto[2]

1 School of Mechanical Engineering, University of Campinas, Campinas, Brazil

2 School of Electrical and Computer Engineering, University of Campinas, Campinas, Brazil

*Address all correspondence to: mvpaula@outlook.com

IntechOpen

References

[1] Hu KW, Yi PH, Liaw CM. An ev srm drive powered by battery/supercapacitor with g2v and v2h/v2g capabilities. IEEE Transactions on Industrial Electronics. 2015;**62**(8): 4714-4727

[2] Bilgin B, Emadi A, Krishnamurthy M. Comprehensive evaluation of the dynamic performance of a 6/10 srm for traction application in phevs. IEEE Transactions on Industrial Electronics. 2013;**60**(7):2564-2575

[3] Mikail R, Sozer Y, Husain I, Islam M, Sebastian T. Torque ripple minimization of switched reluctance machines through current profiling. In: 2011 IEEE Energy Conversion Congress and Exposition. 2011. pp. 3568-3574

[4] Mikail R, Sozer Y, Husain I, Islam M, Sebastian T. Four quadrant torque ripple minimization of switched reluctance machine through current profiling with mitigation of rotor eccentricity problem and sensor errors. IEEE Transactions on Industry Applications. 2015;**5**:2097-2104. DOI: 10.1109/TIA.2014.2365715

[5] Castano SM et al. Acoustic noise analysis of a high-speed high-power switched reluctance machine: Frame effects. IEEE Transactions on Energy Conversion. 2016;**31**:69-77. DOI: 10.1109/TEC.2015.2470079

[6] Krishnan R. Switched Reluctance Motor Drives: Modeling, Simulation, Analysis, Design, and Applications. New York: CRC Press LLC; 2001. 398 p. ISBN 9780849308383

[7] Miller TJE. Switched Reluctance Motors and their Control. Oxford: Oxford Press; 1993. ISBN 0-19-859387-2

[8] Hu Y et al. Split converter-fed srm drive for flexible charging in ev/hev applications. IEEE Transactions on Industrial Electronics. 2015;**62**: 6085-6095. DOI: 10.1109/TIE.2015.2426142

[9] Chang HC, Liaw CM. Development of a compact switched-reluctance motor drive for ev propulsion with voltage-boosting and pfc charging capabilities. IEEE Transactions on Vehicular Technology. 2009;**58**:3198-3215. DOI: 10.1109/TVT.2009.2017546

[10] Hu Y et al. Modular tri-port high-power converter for SRM based plug-in hybrid electrical trucks. IEEE Transactions on Power Electronics. 2017;**33**:3247-3257. DOI: 10.1109/TPEL.2017.2701784

[11] Gan C et al. New integrated multilevel converter for switched reluctance motor drives in plug-in hybrid electric vehicles with flexible energy conversion. IEEE Transactions on Power Electronics. 2017;**32**: 3754-3766. DOI: 10.1109/TPEL.2016.2583467

[12] Lu S, Corzine KA, Ferdowsi M. A new battery/ultracapacitor energy storage system design and its motor drive integration for hybrid electric vehicles. IEEE Transactions on Vehicular Technology. 2007;**56**: 1516-1523. DOI: 10.1109/TVT.2007.896971

[13] Mademlis C, Kioskeridis I. Performance optimization in switched reluctance motor drives with online commutation angle control. IEEE Transactions on Energy Conversion. 2003;**18**:448-457. DOI: 10.1109/TEC.2003.815854

[14] Xue XD et al. Optimal control method of motoring operation for srm drives in electric vehicles. IEEE Transactions on Vehicular Technology. 2010;**59**:1191-1204. DOI: 10.1109/TVT.2010.2041260

[15] Kioskeridis I, Mademlis C. Maximum efficiency in single-pulse controlled switched reluctance motor drives. IEEE Transactions on Energy Conversion. 2005;**20**:809-817. DOI: 10.1109/TEC.2005.853738

[16] Vujicic VP. Minimization of torque ripple and copper losses in switched reluctance drive. IEEE Transactions on Power Electronics. 2012;**27**:388-399. DOI: 10.1109/TPEL.2011.2158447

[17] De Paula M, Barros TAS, Santos No PJ, Ruppert FE. Estudo comparativo de técnicas de minimização de ondulações de torque para motores de relutância variável trifásicos. In: Proceedings of the Congresso Brasileiro de Automática (CBA2018). Brazil; 2018. ISSN 2525–8311

[18] Dowlatshahi M et al. Copper loss and torque ripple minimization in switched reluctance motors considering nonlinear and magnetic saturation effects. Journal of Power Electronics. 2014;**14**:351-361. DOI: 10.6113/JPE.2014.14.2.351

[19] Brauer HJ, Hennen MD, Doncker RWD. Control for polyphase switched reluctance machines to minimize torque ripple and decrease ohmic machine losses. IEEE Transactions on Power Electronics. 2012;**27**:370-378. DOI: 10.1109/TPEL.2011.2161332

[20] Inderka RB, Doncker RWAAD. High-dynamic direct average torque control for switched reluctance drives. IEEE Transactions on Industry Applications. 2003;**39**:1040-1045. DOI: 10.1109/TIA.2003.814579

[21] Hannoun H, Hilairet M, Marchand C. Design of an srm speed control strategy for a wide range of operating speeds. IEEE Transactions on Industrial Electronics. 2010;**57**: 2911-2921. DOI: 10.1109/TIE.2009.2038396

[22] Neto PJ d S, Barros TA d S, de Paula MV, de Souza RR, Filho ER. Design of computational experiment for performance optimization of a switched reluctance generator in wind systems. IEEE Transactions on Energy Conversion. 2018;**33**:406-419. DOI: 10.1109/TEC.2017.2755590

[23] Dos Santos Barros TA, dos Santos Neto PJ, de Paula MV, Moreira AB, Nascimento Filho PS, Ruppert Filho E. Automatic characterization system of switched reluctance machines and nonlinear modeling by interpolation using smoothing splines. IEEE Access. 2018;**6**:26011-26021. DOI: 10.1109/ACCESS.2018.2825607

[24] Petrus V. Switched reluctance motors for electric vehicle propulsion: comparative, numerical and experimental study of control schemes [thesis]. Technical University of Cluj-Napoca & Universitánd Libre de Bruxellesa; 2013

[25] Hyeung S, Kiwoo P, Kyobeum L. A non-unity torque sharing function for torque ripple minimization of switched reluctance generators in wind power systems. Energies. 2015;**8**:11685-11701. DOI: 10.3390/en81011685

[26] Lee DH et al. A simple nonlinear logical torque sharing function for low-torque ripple sr drive. IEEE Transactions on Industrial Electronics. 2009;**56**: 3021-3028. DOI: 10.1109/TIE.2009.2024661

[27] Ye J, Bilgin B, Emadi A. An extended-speed low-ripple torque control of switched reluctance motor drives. IEEE Transactions on Power Electronics. 2015;**30**:1457-1470. DOI: 10.1109/TPEL.2014.2316272

[28] Vujicic VP. Modeling of a switched reluctance machine based on the invertible torque function. IEEE Transactions on Magnetics. 2008;**44**: 2186-2194. DOI: 10.1109/TMAG.2008.2000663

[29] Zhao X, Xu A, Zhang W. Research on dtc system with variable flux for switched reluctance motor. CES Transactions on Electrical Machines and Systems. 2017;**1**:199-206. DOI: 10.23919/TEMS.2017.7961342

[30] Xu AD, He K, Cao Y. Torque ripple reduction of srm using optimized voltage vector in dtc. In: 2016 IEEE Vehicle Power and Propulsion Conference (VPPC). [S.l.: s.n.]. 2016. pp. 1-5

[31] Inderka RB, Doncker RWAAD. Ditc-direct instantaneous torque control of switched reluctance drives. IEEE Transactions on Industry Applications. 2003;**39**:1046-1051. DOI: 10.1109/TIA.2003.814578